Testing of the CubeSat Laser Infrared CrosslinK (CLICK-A) Payload

Ondrej Čierny, Paul Serra, William Kammerer, Peter Grenfell, Grant Gunnison, Joseph Kusters, Cadence Payne, Paula do Vale Pereira, Kerri Cahoy
Dept. of Aeronautics and Astronautics, Massachusetts Institute of Technology, Cambridge, MA, USA
ondrej@mit.edu

Tyler Ritz, John Conklin
Dept. of Mechanical and Aerospace Engineering, University of Florida, Gainesville, FL, USA

David Mayer, Jan Stupl
NASA Ames Research Center, Moffett Field, CA, USA

John Hanson
CrossTrac Engineering, Mountain View, CA, USA

Abstract

The CubeSat Laser Infrared CrosslinK (CLICK-A) is a risk-reduction mission that will demonstrate a miniaturized optical transmitter capable of ≥10 Mbps optical downlinks from a 3U CubeSat to a portable 30 cm optical ground telescope. The payload is jointly developed by MIT and NASA ARC, and is on schedule for a 2020 bus integration and 2021 launch. The mission purpose is to reduce risk to its follow-up in 2022, called CLICK-B/C, that plans to demonstrate ≥20 Mbps intersatellite optical crosslinks and precision ranging between two 3U CubeSats. The 1.4U CLICK-A payload will fly on a Blue Canyon Technologies 3U bus inserted into a 400 km orbit. The payload will demonstrate both the transmitter optoelectronics and the fine-pointing system based on a MEMS fast steering mirror, which enables precision pointing of its 1300 μrad full-width half-maximum (FWHM) downlink beam with an estimated error of 136.9 μrad (3-σ) for a pointing loss of -0.134 dB (3-σ) at the time of link closure.

We present recent test results of the CLICK-A payload, including results from thermal-vacuum testing, beam characterization, functional testing of the transmitter, and thermal analyses including measurement of deformation due to the thermal loading of the MEMS FSM.

1 Introduction

As increasingly data-intensive instruments are flown on small spacecraft, such as multiband radiometers or hyperspectral cameras, the downlink rate requirement of their miniaturized transmitters is steeply increasing. Several planned CubeSat missions will generate raw data on the order of several terabytes per day.[1] Laser communications (lasercom) offers a scalable solution to this growing downlink demand due to its efficiency in terms of size, weight, and power consumption.

The CubeSat Laser Infrared CrosslinK (CLICK) is a joint project involving MIT, University of Florida (UF), and NASA Ames Research Center (ARC), focused on demonstrating laser downlinks and crosslinks between nanosatellites using low-cost, miniaturized optical transceivers in a CubeSat form factor. The ultimate vision of the technology demonstration is to enable large constellation or swarms of nanosatellites that are interconnected with optical communications.

The first flight of the CLICK mission, called CLICK-A, is a risk-reduction 1.4U payload for a 3U spacecraft that will demonstrate a ≥10 Mbps optical downlink to a portable 30 cm optical ground telescope. The primary objective of CLICK-A is to reduce risk to its follow-up flight in 2022, called CLICK-B/C, that will demonstrate ≥20 Mbps intersatellite optical crosslinks and precision ranging between two 3U CubeSats. CLICK-A will verify both the transmitter optoelectronics and a custom fine-pointing mechanism based on a MEMS fast-steering mirror (FSM). The payload uses a master-oscillator power-amplifier (MOPA) transmitter design at 1550 nm with a commercial-off-the-shelf (COTS) Erbium-Doped Fiber Amplifier (EDFA). For pointing, acquisition, and tracking, a 975 nm uplink beacon is captured by a camera and tracked with the FSM, enabling 136.9 μrad (3-σ) precision pointing of its 1300

μrad full-width half-maximum (FWHM) downlink beam for a pointing loss less than -0.134 dB.

The CLICK-A payload is currently in its final testing phase before its planned late summer 2020 integration with a 3U Blue Canyon Technologies (BCT) spacecraft bus. In this paper, we present the most recent payload testing results and analyses, including thermal-vacuum testing of the payload optical system, developments and lessons learned in the optomechanical design of the payload and the optical ground station, updated thermal analysis, and results from the transmitter optoelectronics testing.

2 Link Analysis and Experiment Operations

In this section, the CLICK A concept of operations (ConOps) will first be presented. Next, operations and link analysis for downlink experiments will be presented. Lastly, the pointing budget analysis used as part of the link analysis will be discussed. Figure 1 shows the CLICK A ConOps. The spacecraft will be deployed from the International Space Station (ISS) into low Earth orbit (LEO) via NanoRacks. Following deployment, daily S-band radio links will be established using three KSAT lite ground antenna stations, which will relay telemetry, tracking, and command (TTC) data between the spacecraft and the mission operations center (MOC) located at MIT. All spacecraft operations, including downlink experiments, will be scheduled via ground commands issued by the MOC. Optical downlink experiments will be performed using an optical ground station (OGS) located at MIT Wallace Astrophysical Observatory. The OGS is called the Portable Telescope for Lasercom (PorTeL) and is briefly described further in Section 7 and described in detail in other references.[2,3]

A downlink experiment can be decomposed into several stages. For reference, define t_0 as the time at the beginning of the overpass at which the spacecraft elevation angle with respect to the ground station is zero. At $t = t_0 - 15$ minutes, the lasercom payload is turned on and performs initial boot up steps, with a measured payload power draw of 3.95 W. At the same time, the Blue Canyon Technologies (BCT) spacecraft bus executes an attitude control sequence to begin pointing the payload's aperture at the ground station's geodetic coordinates. At t_0, the 200 mW, 1550 nm payload laser is activated with an estimated payload power draw of 17.5 W for the remainder of the pass. After the pass, the payload will perform necessary shut down activities for 2 minutes with a measured payload power draw of 3.95 W until it is scheduled to be switched off by the spacecraft bus.

As will be described in Section 2.2, it is not expected that the downlink to the OGS will close until the payload's closed-loop fine pointing stage is enabled. This will occur when the 5 W, 975 nm uplink beacon laser from the OGS is detected by the payload's camera. In nominal operations, the OGS will be pointing at the payload by tracking an ephemeris generated by Global Positioning System (GPS) receiver telemetry from aboard the spacecraft, which will be discussed further in Section 2.2. This phase of pointing, acquisition, and tracking (PAT) for the OGS is called coarse stage tracking in open-loop (CSTOL) because it uses the coarse pointing stage of PorTeL (the telescope gimbals) without any need for optical closed-loop feedback from the spacecraft. Once the beacon uplink is acquired by the payload fine pointing sensor (e.g. its camera), fine stage tracking (FST) on the spacecraft side is activated, which utilizes the payload's Mirrorcle fine/fast steering mirror (FSM) controlled by measuring the error offset between the beacon spot and the spot generated by an on-board calibration laser (see Figure 6). Upon activation of fine pointing, the downlink to the ground station's near-infrared (NIR) tracking camera will close, and the next OGS PAT stage will activate: coarse stage pointing in closed-loop (CSTCL). This enables the OGS to track the laser signal from the spacecraft for the remainder of the pass rather than continuing to rely on an ephemeris. Finally, the last OGS PAT stage will activate: fine stage tracking (FST). This utilizes a FSM shown in Figure 23. The FSM is controlled using the tracking camera signal, and the coarse tracking control is transitioned from using the tracking camera error signal to offloading the FSM: pointing the telescope to attempt to minimize the commanded control angles sent to the FSM. During FST, the received signal from the spacecraft is centered on the communications receiver (an avalanche photodiode detector (APD)), and an oscilloscope is used to sample data from the APD throughout the pass for offline analysis to validate the mission's communications requirement of a ≥ 10 Mbps downlink.

2.1 Downlink Analysis

An important part of downlink analysis is determining the details of the time-varying relative geometry of the spacecraft overpass. This was analyzed using AGI's System's Tool Kit (STK) to simulate overpasses of the OGS location at Wallace (latitude $= 42.610554°$, longitude $= -71.483833°$) from an ISS LEO orbit. The first step was to perform a sur-

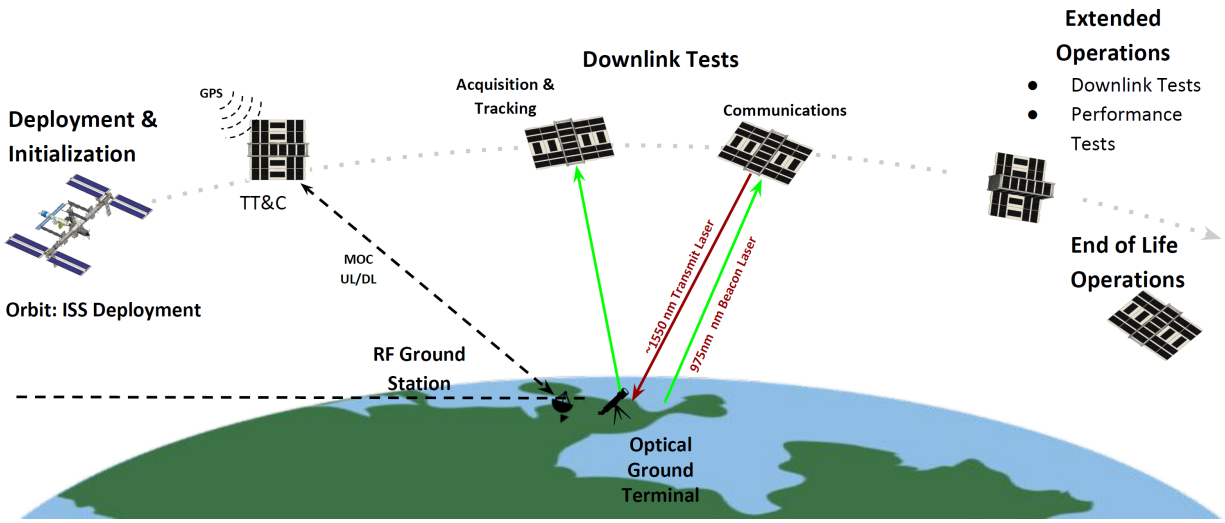

Figure 1: CLICK A Mission Concept of Operations.

vey of overpasses over an extended time frame. This was done by propagating the orbit over 3 years starting from an epoch at June 07, 2020 at 12:56:15.000 UTC. This time period includes expected on-orbit operations for CLICK A, the specific launch epoch of which is to be determined as of this writing. The main analysis objective was was to simulate a variety of reasonably accurate passes to survey four overpass metrics: pass duration, maximum elevation during the pass, minimum range between the S/C and the OGS during the pass, and whether or not the pass occurred during eclipse. A J_2 force model was used to generate precession of the orbit's ascending node (Ω) to acheive a variety of passes. Additional perturbations were ignored because the ISS performs station keeping for orbit maintenance, so the semi-major axis (a), eccentricity (e), and inclination (i) are assumed to be stable over time. The argument of perigee (ω_p) is less important than these three elements since the orbit is nearly circular. Lastly, the exact value of the mean anomaly (M) is not important for this analysis since the objective was not to predict pass times for operations; however, that capability will be developed further as part of ongoing development of the mission operations software. The orbital elements used at epoch were pulled from an online reference for the ISS's orbit:[4] ($a = 6796.7\text{km}, e = 2.243 * 10^{-4}, i = 51.645°, \Omega = 36.233°, \omega_p = 27.871°, M = 332.26°$). During the survey simulation, Sun and Moon keep out constraints were imposed for access computations: the payload's keep out half-angle was defined to be 95° since it does not have any baffling for stray light protection, and the telescope's keep out half-angle was estimated to be 45° based an inspection of the baffling contained in its bore following its secondary mirror; however, further testing with the hardware is needed to verify both of these values.

The survey yielded 7435 overpasses; however, not all of these are deemed to be desirable based on the four metrics, so these were downselected to only include passes that have a minimum pass duration of 1 minute, a maximum pass elevation between 20° and 80°, a minimum pass range of less than 1000 km, and a pass time that occurs while the OGS is in eclipse. The duration requirement is primarily based on the need for a human operator for the OGS to monitor the system, which would be difficult for an extremely brief pass. The maximum pass elevation requirements are based on two things. First, there are obstructing trees and buildings around the OGS in addition to uplink beacon laser safety concerns that mean that a pass below 20° is impractical and potentially unsafe to track. Second, as noted by Riesing in her testing, the gimballed telescope is subject to the well-known keyhole problem, which means that the azimuth rate increases dramatically for high elevation passes.[2] This can exceed the capabilities of the azimuth gimbal motor, causing the OGS to lose track of the spacecraft. Although 80° is still a relatively challenging pass, PorTeL has successfully tracked the ISS for passes up to 80° in past tests, so this was set as the upper bound. Finally, based on preliminary link analysis, it was determined that a pass with a minimum range less than 1000 km is effectively guaranteed to succeed barring unfore-

seen variations in other link parameters. Finally, since neither the payload nor the ground station are designed to effectively capture and attenuate high-intensity stray light from close approaches to the sun (or moon to a lesser extent), only passes where the ground station is in eclipse (i.e. at night) were allowed in addition to the keep out requirements already levied. With these four requirements, 1746 "good" passes were selected, which accounts 23.5% of all passes. The average number of good passes per day is 1.59, and the average waiting time between these passes is 15.03 hours. Of course, these metrics are dependent on the pass requirements levied, which will be further tuned for actual operations.

For link analysis, a single pass approximately one year from the survey epoch with good characteristics was selected. For the purposes of this work, a single good pass is sufficient to illustrate all the relevant features of a downlink. Although a statistical link analysis of all good passes would also be useful, at present the link analysis software run time is not efficient enough to make that practical, so that more comprehensive analysis is relegated to future work. The reference pass epoch was July 09, 2021 at 03:52:15.000 UTC, with the following orbital elements at epoch: $(a = 6791.3\text{km}, e = 6.084{*}10^{-4}, i = 51.483°, \Omega = 221.52°, \omega_p = 181.99°, M = 220.44°)$. The pass duration was 10.90 minutes, the maximum pass elevation was 53.99°, the minimum pass range was 517.60 km, and the pass occurred during eclipse of the OGS. The link budget parameters for the three link sensors (OGS-APD, OGS-Camera, S/C-Camera) are given at the minimum pass range in Table 1, and the variations of the most important link parameters during the pass are given in Figures 2 - 5. Table 1 shows the fixed link parameters as well as the variable link parameters captured at minimum range. The fixed parameters include the transmitter implementation loss ($L_{\text{Tx,imp}}$) and the receiver implementation loss ($L_{\text{Rx,imp}}$), which are both computed based on optical coating and fiber losses in the relevant optical trains. There is a noticeable receiver loss for the OGS-camera, which is due to the use of a 90 : 10 beam splitter, which reflects 91.2% of the incident light to the APD and transmits 8.2% of the light to the OGS camera. This optimizes the system for communications link performance while retaining sufficient tracking link performance. The atmospheric loss term is based on an analysis carried out in MODTRAN (L_{atm}). The margin associated with PPM32 is given here since this is the maximum PPM order that enables a $\geq$ 10 Mbps downlink to satisfy the mission requirement. Additional results with other PPM orders are shown in Figure 5 and Table 2. A step-by-step discussion of the analysis involved in computing each link term is beyond the scope of this work; however, further discussion of the equations used for each link budget term can be found in Grenfell,[5] Casey & Lambert,[6] Clements,[7] Clements et al.,[8] and Kingsbury.[9]

Figure 2 shows the received power for each of the three sensors over the duration of the pass as well as the link ranges during the pass. The received power for the OGS sensors are restricted to the time period defined by closed loop tracking of the downlink laser, which begins simultaneously with the closure of the beacon uplink to the S/C camera at 1.67 minutes into the pass at a range of 1699.8 km. The criteria for link closure for the pointing sensors (the cameras) is that the SNR margin is $\geq$ 0 dB, which is shown in Figure 4. There is a noticeable jump in the received power from -124 dBW to -122 dBW by the S/C-cam at this time that comes from transitioning from open-loop to closed-loop tracking of the spacecraft by the OGS. As would be expected, the maximum received powers are acheived at the minimum range, and these are summarized in Table 1. Lastly, the uplink (and hence the downlink) is lost at 9.58 minutes into the pass at the same limiting range of 1699.8 km.

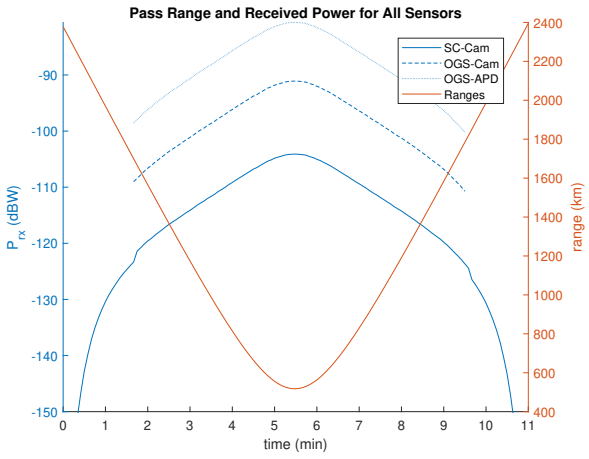

Figure 2: Link range and received power for all sensors for a reference overpass.

The pointing loss (L_{ptg}) on both the uplink and the downlink are also variable. The computation of pointing loss will be discussed in Section 2.2, and the behavior during the pass is given in Figure 3. The uplink pointing loss is due to mispointing error of the ground beacon laser by the OGS. The main variable in this budget is the link range, which is used to divide the ephemeris position error to generate an angular pointing error; hence, the inverse relationship

Table 1: Downlink experiment link budgets at the minimum range of the reference overpass.

Link Parameter	OGS-APD		OGS-Camera		S/C-Camera	
P_{Tx} (dBW)	-6.99	200 mW avg.	-6.99	200 mW avg.	6.99	5 W
G_{Tx} (dB)	68.17	2208 μrad $1/e^2$	68.17	2208 μrad $1/e^2$	55.51	9487 μrad $1/e^2$
G_{Rx} (dB)	115.1	28 cm Aper.	115.1	28 cm Aper.	94.47	16.4 mm Aper.
L_{path} (dB)	-252.5	517.60 km	-252.5	517.60 km	-256.5	517.60 km
$L_{\mathrm{Tx,imp}}$ (dB)	-1.46	CBE	-1.46	CBE	-1.02	CBE
$L_{\mathrm{Rx,imp}}$ (dB)	-0.82	CBE	-11.27	CBE	-1.44	CBE
L_{ptg} (dB) (99.7%)	-0.06	91.8 μrad	-0.06	91.8 μrad	-0.04	304.7 μrad
L_{atm} (dB)	-2.10	el = 53.99°	-2.10	el = 53.99°	-2.10	el = 53.99°
P_{Rx} (dBW)	-80.64		-91.09		-104.11	
$P_{\mathrm{Rx,bkgd}}$ (dBW)	-181.6	eclipse	-169.0	eclipse	-224.7	eclipse
Metric	-80.64	P_{Rx} (dBW)	29.56	SNR (dB)	29.15	SNR (dB)
Requirement (dB)	-85.25	P_{req} - PPM32	8.25	$\mathrm{SNR}_{\mathrm{req}}$	9.75	$\mathrm{SNR}_{\mathrm{req}}$
Margin (dB)	4.61		21.32		19.41	

1550 nm Tx to OGS-APD & OGS-Camera. 975 nm Beacon to S/C-Camera.

with range: the pointing error goes up as the range decreases. This behavior abrubtly changes when the uplink and downlink close because the OGS transitions to closed loop tracking. The variable element in closed loop tracking is the noise equivalent angle (NEA) error of the tracking sensor, which is determined by the signal-to-noise ratio (SNR). The SNR improves with increasing power, so the pointing loss for both the uplink and the downlink improve slightly with reductions in range; however, due to the nature of the root-squared-sum that is used to compute the total error covariance, the relatively small variations in NEA only lead to small variations in pointing error of about 0.078 dB for the downlink loss and 0.0046 dB for the uplink loss during closed-loop tracking.

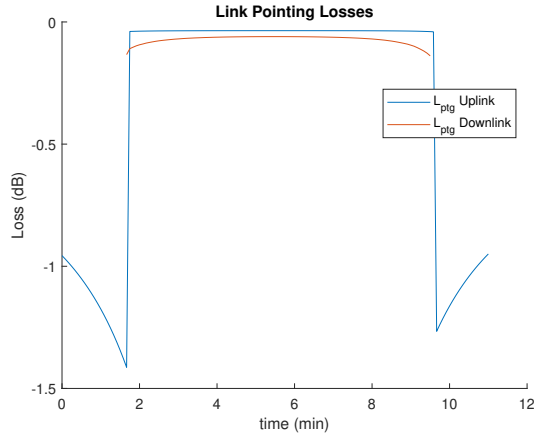

Figure 3: Link pointing losses for a reference overpass.

As mentioned, the SNR margin criterion for link closure to the pointing sensors is given in Figure 4. As would be expected, the SNR increases as range decreases and received power increases. The intersection point of the 0 dB line with the S/C-Cam SNR margin defines the link closure time of 1.67 minutes. The SNR margin is computed as the difference between the SNR computed from the link budget and a theoretical SNR requirement for the peak power point on the sensor using Equations 1a - 1b.[10] TNR is the threshold-to-noise ratio computed as a function of the false-alarm rate (FAR [Hz]) and the sensor bandwidth (f [Hz]). Following the approach taken by Yura,[10] the FAR is set to $3.171 * 10^{-8}$ Hz, which is 1 per year. The bandwidth of the S/C camera is 30 Hz,[11] and the bandwidth of the OGS camera is 0.5 Hz,[2] though these rates are adjustable by changing the camera's integration time setting. These correspond to TNRs of 8.02 dB and 7.53 dB, respectively. The detection probability (P_d) is set to 99.9%, which yields the SNR requirements given in Table 1.

$$\mathrm{TNR} = \sqrt{-2\ln\left(\sqrt{3}\mathrm{FAR}/f\right)} \tag{1a}$$

$$\mathrm{SNR}_{\mathrm{req}} = \sqrt{2}\mathrm{erf}^{-1}\left(2P_d - 1\right) + \mathrm{TNR} \tag{1b}$$

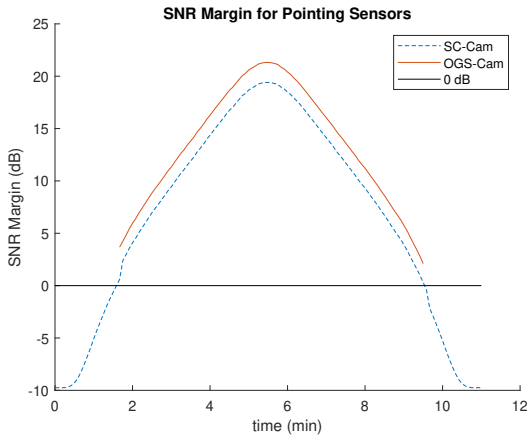

Figure 4: SNR margins for pointing sensors for a reference overpass.

Finally, Figure 5 shows the range variation of margins for communications at various pulse-position-modulation (PPM) orders. Higher PPM orders have lower data rates (see the plot legend) and reduced requirements, which leads to higher margins. All PPM orders achieved positive margins during the pass, including PPM orders of 32 or less, which are needed to achieve data rate $\geq$10 Mbps in order to satisfy the mission requirement. To get an idea of the amount of data it is theoretically possible to transfer with each of the PPM orders, the communications durations for each PPM order were computed. The results are summarized in Table 2. The optimal PPM order for this pass would be PPM16 since it achieved the maximum data transfer of 4.507 Gb. A dynamic PPM would enable further optimization of data transfer. For example, if PPM order were to be adjusted to give the best available data rate throughout the pass, then the total data transfer would be 7.916 Gb.

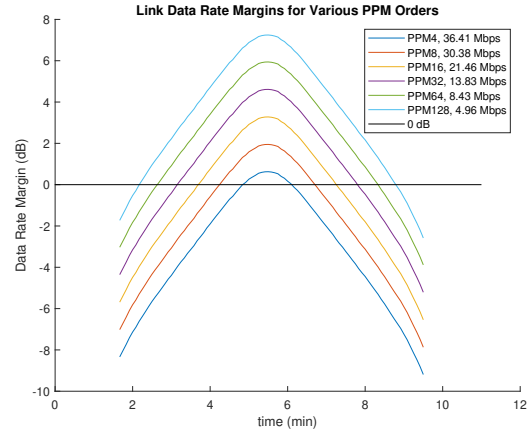

Figure 5: Downlink data rate margins for a reference overpass for various PPM orders.

Table 2: Communications metrics for a reference overpass.

PPM	Data Rate (Mbps)	Duration (s)	Data Transfer (Gb)
4	36.41	70	2.549
8	30.37	145	4.405
16	21.46	210	4.507
32	13.83	275	3.803
64	8.43	340	2.865
128	4.96	390	1.933

In this section, the results of a survey of overpasses of the CLICK A OGS location from a LEO ISS orbit were used to downselect passes satisfying four metrics: a minimum pass duration of 1 minute, a maximum pass elevation between 20° and 80°, a minimum pass range of less than 1000 km, and a pass time that occurs while the OGS is in eclipse. 23.5% of passes satisfied these metrics with an average waiting time between these types of passes of 15.03 hours. A single reference pass was selected for link analysis with a pass duration was 10.90 minutes, maximum pass elevation of 53.99°, minimum pass range of 517.60 km, and occurring during eclipse of the OGS. Link analysis showed that the beacon uplink budgets closed for a duration of 7.91 minutes. Furthermore, all the communications downlink closed with margin for PPM orders 4 to 128 during the pass with respective durations between 1.17 minutes and 6.5 minutes. The mission requirement of $\geq$10 Mbps is satisfied for PPM orders less than 32. Furthermore, PPM 16 acheived the best theoretical data transfer for a fixed PPM order of 4.507 Gb. Lastly, an improved data transfer of 7.916 Gb could be achieved by optimal variation of the PPM order during the pass.

2.2 Downlink Pointing Budgets

There are three separate laser pointing budgets that are used to analyze pointing loss for the downlink experiment link budgets. The pointing budgets for the OGS beacon laser when operating in open-loop (CSTOL) and closed-loop (CSTCL) coarse stage tracking modes are given in Tables 3 & 4, respectively. The pointing budget for the payload laser during fine stage tracking (FST) is given in Table 5. In these tables, $\Theta_{\text{ptg}} = \sqrt{\Theta_x^2 + \Theta_y^2} \sim \text{Rice}(\sqrt{2}\mu, \sigma)$ is the total two-axis pointing error, with μ and σ being the Gaussian parameters of the sum of the single axis pointing error components: $\Theta_x \sim N(\mu, \sigma)$ & $\Theta_y \sim N(\mu, \sigma)$. These are conservatively modeled as symmetric Gaussian random variables by using the worst case axial pointing error component when

geometric asymmetries are present in the error components. The pointing loss computation is discussed further in Section 7.2 when the mathematics of divergence optimization is discussed. The reader is referred to Grenfell for an in-depth discussion and derivation of the statistical pointing budget models used here.[5]

Table 3: Pointing error budget for OGS beacon coarse stage tracking in open-loop (CSTOL) at time of uplink/downlink closure (2.25 min, 1466.5 km).

Budget Element	μ (μrad)	σ (μrad)
Satellite Ephemeris	0	456.5
OGS Star Tracker Calibration	0	315.1
Gimbal Pointing Jitter	0	85.11
Open-Loop Point Ahead	12.24	4.93
Beacon Alignment Residual	0	6.39
Total	12.24	561.3
θ_{1/e^2} (μrad)	9487	
θ_{ptg} (μrad, $p_\theta = 0.997$)	1914	
$L_{\text{ptg,dB}}$ (dB, $p_l = 0.997$)	-1.414	

In Table 3, the dominant error term is the satellite ephemeris error. This was computed based on an analysis of SGP4-based batch least squared differential correction orbit determination errors using GPS telemetry. The details of this analysis are beyond the scope of the present work and will be published as part of a future work; however, the concept and previous results can be found in the literature.[12–14] This analysis yielded an anticipated position error of 0.776 km (1-σ), which when divided by the link range gives the angular error. The OGS star tracker calibration and gimbal pointing jitter values are based on experimental data from the PorTeL prototype units.[2,3] Point ahead error is the error associated with the finite speed of light, similar to how the finite speed of any projectile must be taken into account when attempting to hit a target. The formula for point ahead error in open-loop is $\theta_{\text{PA}} = v_{\text{rel,perp}}/c$, where $v_{\text{rel,perp}}$ is the magnitude of the component of the relative velocity between the transmitter and the receiver that is orthogonal to the line of sight. In closed-loop, this error doubles because there is a contribution from the target's laser signal in addition to the transmitter's laser signal. The values used here are based on previous a statistical analysis of point ahead error for LEO orbit downlinks.[5] Lastly, the beacon alignment residual is determined by the accuracy of the calibration procedure, which involves using a retroreflctor with a 3 arcsec beam deviation to shine the beacon back into the telescope and register it on the tracking camera. The beacon is the adjusted in tip/tilt using a kinematic mount until it is centered on the camera, which contributes an additional error residual based on the centroiding accuracy of the camera.

Table 4: Pointing error budget for OGS beacon coarse stage tracking in closed-loop (CSTCL) at time of uplink/downlink closure.

Budget Element	μ (μrad)	σ (μrad)
OGS Camera NEA	0	26.88
Gimbal Pointing Jitter	0	85.11
Closed-Loop Point Ahead	24.48	9.859
Beacon Alignment Residual	0	6.39
Total	24.48	90.02
θ_{1/e^2} (μrad)	9487	
θ_{ptg} (μrad, $p_\theta = 0.997$)	317.3	
$L_{\text{ptg,dB}}$ (dB, $p_l = 0.997$)	-0.039	

For Table 4, the OGS is operating in closed-loop, so coarse stage tracking is no longer dependent on the satellite ephemeris or external calibration. These are replaced by the error from the tracking camera measurements of the received laser signal, which is defined using the noise equivalent angle. The formula for this is NEA $= 1/(\text{SF} * \sqrt{\text{SNR}})$, where SF is the slope factor of the sensor, which for a Gaussian spot is given as SF $= 1.56/\theta_{\text{spot}}$.[6] θ_{spot} is the angular size of the spot, which is computed based on the radius of the first minimum of an Airy disk: $\theta_{\text{spot}} = 2.44\lambda F\#/f$.[6] The remaining distinction between open-loop and closed-loop is the point ahead, which as previously noted is doubled in closed-loop.

Table 5: Pointing error budget for payload fine stage tracking at time of uplink/downlink closure.

Budget Element	μ (μrad)	σ (μrad)
S/C Camera NEA	0	28.23
Bus Reaction Wheel Jitter	0	1.45
Closed-Loop Point Ahead	24.48	9.859
FSM Control Residual	0.31	16.4
Total	24.79	34.14
θ_{1/e^2} (μrad)	2208	
θ_{ptg} (μrad, $p_\theta = 0.997$)	136.9	
$L_{\text{ptg,dB}}$ (dB, $p_l = 0.997$)	-0.134	

As seen in Table 5, the pointing error for fine stage tracking on the spacecraft side has similar error contributors as that of the closed-loop coarse stage tracking for the ground station. The NEA is defined and computed in the same way based on the parameters of the payload's camera and the uplink SNR. The jitter term comes from the spacecraft's reaction wheels, which are running throughout the pass in order for the spacecraft bus to point the payload aperture at the ground target. The estimate here is based on results from ASTERIA, which also used a BCT bus, with a factor of safety of 3.[15] The FSM

control residual error is based on hardware testing carried out at MIT.[11]

Finally, there are also analyses to determine the probability of acquisition given the field of view (FOV) of the sensors. For brevity, the tables associated with these analyses are omitted as the FOV's are all sufficiently large to virtually guarantee acquisition given the magnitudes of errors described in the pointing budgets. The OGS camera has an FOV of $\pm 3484\mu$rad and a single-axis aperture open-loop tracking pointing error distributed as $N(0, 561.2)\mu$rad, which yields an acquisition probability at the time of downlink closure of 100% when rounded for significant figures. The OGS APD has an FOV of $\pm 217.9\mu$rad with an associated closed-loop tracking pointing distribution of $N(0, 32.6)\mu$rad, which also yields an acquisition probability of 100%. Lastly, the S/C camera has an FOV of $\pm 92707\mu$rad and an associated aperture pointing distribution of $N(0, 2095)\mu$rad, which again yields an acquisition probability at the time of uplink closure of 100%. The aperture pointing error consists of errors from onboard relative navigation ($N(0, 2.674)\mu$rad[5]), measurement error of the misalignment between the payload fiducial and the spacecraft's star tracker fiducial ($N(0, 484.8)\mu$rad), alignment error of the payload camera relative to the payload fiducial ($N(0, 2034)\mu$rad), and the error associated with the spacecraft's attitude control system ($N(0, 122.2)\mu$rad[16]). The dominant error source is misalignment of the payload fiducial relative to the camera, which is estimated based on mechanical tolerances of the assembly. Due to the large FOV of the camera, it is unnecessary to reduce these misalignment errors for acquisition. However, if one uses these errors to compute pointing loss for an attempted open-loop laser pointing manuever, one finds that the loss is sufficiently large to break the downlink at acquisition ranges. This is why open-loop pointing of the spacecraft laser is not considered in the previous link analyses. It may be possible to use the payload's FSM to offset these misalignment errors by scanning; however, the analysis for this is beyond the scope of the present work and is relegated to future work.

In this section, the pointing budget analysis for the OGS beacon laser when operating in open-loop (CSTOL) and closed-loop (CSTCL) coarse stage tracking modes are given as well as the pointing budget for the spacecraft transmit laser operating in fine stage tracking (FST) mode. The 9487μrad $1/e^2$ (0.32° FWHM) uplink beacon divergence coupled with open-loop and closed-loop $3-\sigma$ pointing errors of 1914μrad and 317.3μrad yielded pointing losses of -1.414 dB and -0.039 dB at the time of uplink acquisition. Upon uplink acquisition, the 2208μrad $1/e^2$ (1300μrad FWHM) transmit laser divergence coupled with a closed-loop $3-\sigma$ pointing error of 136.9μ rad yielded a pointing loss of -0.134 dB at the time up uplink acquisition, which is also the time of downlink closure.

3 Payload Optical Testing

The payload optical system can be divided into two subsystems: the beacon receiver optics and the transmitter optics. The beacon receiver consists of a silicon CMOS camera and a COTS lens assembly. The transmitter optics include a laser collimator and the MEMS FSM for precision steering of the transmit beam. The performance of the transmitter pointing system was evaluated in previous experiments, which confirmed pointing loss less than -0.48 dB.[17] Additionally, the optics include a dichroic filter for wavelength separation and a double bandpass filter at the payload aperture for stray light isolation. A top view CAD of the optical system can be seen in Figure 6.

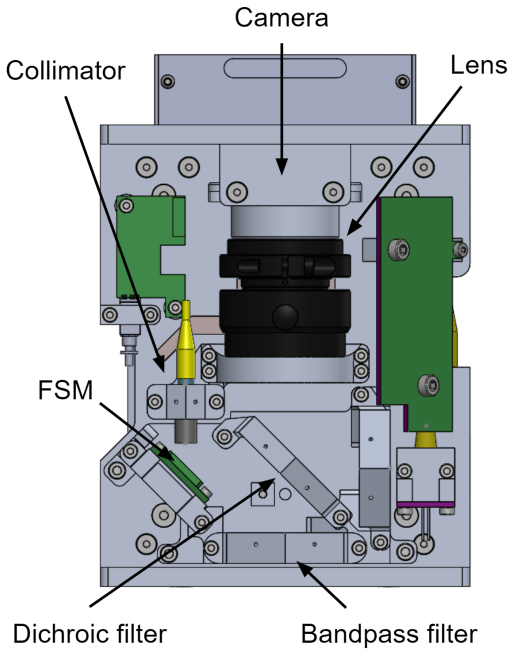

Figure 6: Top view of the CLICK-A payload

3.1 Beacon Receiver TVAC Test

The CLICK-A and B/C payloads use the same camera (mvBlueFOX-MLC205G-XOW-2111) and lens assembly (Schneider Xenoplan 1.4/23-0902) to acquire and track the location of the tracking beacon

for aligning the transmitting laser. Given that these parts are both COTS components not designed for use in space, the project underwent space qualifying this camera and lens for its use in a relevant space environment such as the one that will be seen during the operation of these payloads. For this reason, a thermal-vacuum (TVAC) test campaign was conducted to verify the beacon receiver performance, specifically to verify that the point spread function (PSF) would not degrade over temperature.

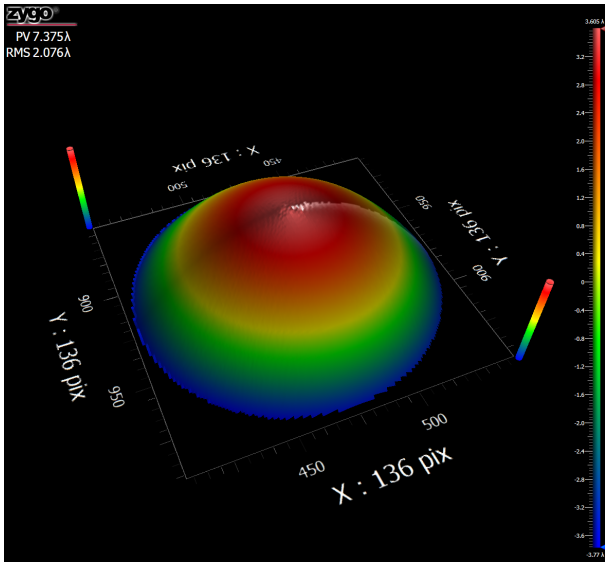

Figure 7: Zygo measurement of the double-bandpass coated surface

To test the camera and lens, they were affixed together, as they would be in flight, and focused. The conjoined lens and camera were mounted in the the CLICK-A payload structure to assure the performance would similar to how it would be operated by our payload in space. The original plan was to test the full optical train of the CLICK-A payload, but the team ran into issues will setting up the test. With the lens focused before being mounted in the payload, the lens and camera would create a diffraction-limited PSF if a plane wave was input into the lens. As the other optics in the optical train of the payload were mounted, it was observed that the addition of the double bandpass filter, that only passes 1550nm and 976nm light, in the payload caused the diffraction limited PSF on the camera to spread. It was theorized that this double bandpass filter was acting as a lens and influencing the collimated light coming into the payload. To investigate, the filter was mounted in front of a Zygo interferometer, which was able to confirm that the filter was acting as a weak lens. As it turns out, the bandpass filter we had purchased was only coated on one side, which created stresses on one side of the filter and caused the filter substrate to flex, turning it into a weak lens. The Zygo measurement of the coated side of bandpass filter can be seen in Figure 7, confirming a curvature of several wavelengths. In order to compensate for this, the Schneider lens needs to be refocused before the final flight integration.

Because of the curvature, the bandpass filter was omitted from the initial beacon receiver TVAC lens test. The rest of the assembled optics and structure were mounted to a fixture plate that allowed them to rest inside a temperature controlled highly emissive shroud inside the vacuum chamber that was used. The payload optics and structure is shown mounted to the fixture plate in Figure 9. The assembly was cooled using radiative coupling form the cool shroud while heating was accomplished using a 22 W heater in a simulated position of the optical amplifier of the payload. The temperature of the components of the test were monitored using RTD temperature sensors.

The payload optics, structure, and fixture were mounted in the TVAC chamber with a window on the top of it that allowed collimated light to be transmitted into the boresight of the lens and camera. A picture of the test chamber is shown in Figure 9.

The chamber was allowed to pump down for 24 hours then the testing began. The initial pump down confirmed the survival of the lens in a vacuum environment. The performance of the camera and lens was measured through the temperature range of -40° C to 40° C. The data of the TVAC testing showed that the point spread function of the lens was suitable for centroid tracking of the spot over the temperature range. Shown in Figure 10, the X and Y dimension PSF diameter can be seen over temperature compared to the diffraction limit.

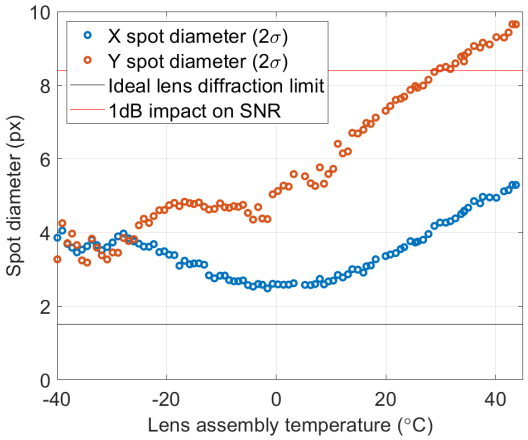

Figure 10: Gaussian fit of PSF vs. TVAC temperature

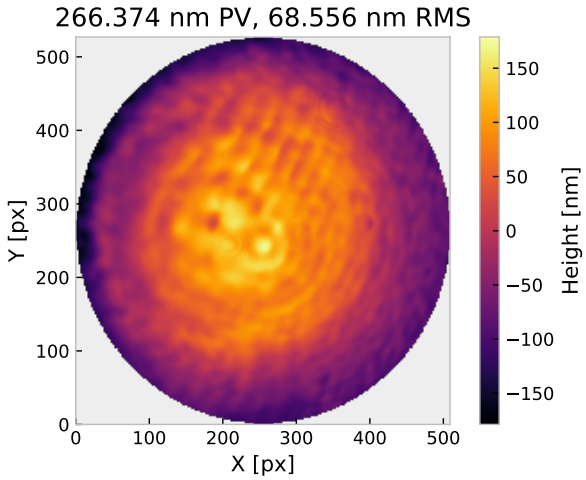

Figure 11: FSM surface deformation measurement, showing peak-to-valley (PV) and root-mean-square (RMS) surface irregularity

It can be seen that with changing temperature, the lens assembly undergoes some defocus in vacuum, given the change in the PSF diameter. However, the change is so small that the impact on the beacon receive link is almost negligible (sub 1 dB below 30° C). It was also observed that the centroiding algorithm worked without any issues over the entire range, without the need of adapting exposure time on the camera to compensate the PSF spreading.

3.2 FSM Thermal Load Test

The next two optical tests focused on the transmitter related optics. With regards to environmental testing, we were interested in the effect of thermal loading on the miniature MEMS FSM and its ability to dissipate heat that is partially absorbed from the high-power transmit laser. To facilitate this, the payload FSM was shipped to be tested in a TVAC interferometry setup at Facebook Connectivity Lab, which has done a lot of testing on thermal loading of MEMS FSMs.[18] The aluminum-coated FSM and our flight transmit collimator were used to irradiate the mirror surface in vacuum using an EDFA-amplified 1550 nm laser source. The test was performed at a pressure of $3 * 10^{-5}$ Torr, with a 30 sec irradiance with up to 250 mW.

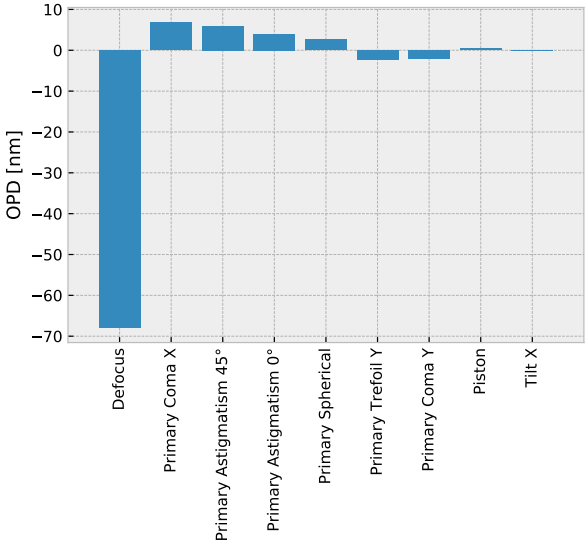

Figure 12: Breakdown of beam aberrations resulting from a thermally-deformed FSM

Figures 11 and 12 show the results of the thermal loading test obtained from a Zygo interferometer after a 30 sec irradiation at 200 mW. The surface figure plot shows a quite noticeable curvature, with a peak-to-valley (PV) displacement of 266 nm. A breakdown of the first few Zernike terms contributing to the beam aberration shows the majority is in defocus. The measured deformations were injected into the payload Zemax model, and an analysis was run using the physical optics propagator to evaluate the impact on the transmit beam divergence. For the CLICK-A payload, the change in beam divergence resulting from the mirror deformation is on

the order of 2 μrad and has very little impact on our transmit gain (0.02 dB change) and link budget. However, for terminals with narrower beams utilizing MEMS FSMs, this might pose an issue that has to be compensated.

3.3 Transmit Beam Divergence Test

Although the deformed FSM is not expected to contribute to spreading of the transmit beam, the curved bandpass filter, which showed a curvature of several wavelengths, is a more serious problem in terms of transmit beam spreading. To verify that the impact on the transmit gain is within margins, a beam divergence measurement was performed using a Thorlabs beam profiler (BP209-IR). Two beam waist measurements were taken with a separation of 1 meter and compared with predicted beam waist diffraction given the manufacturing specification of both the fiber and the transmit collimator, both of which have some uncertainty in their parameters. The results are summarized in Figure 13, which confirms that the beam is within specification, and that the degradation due to the bandpass filter curvature is negligible in terms of beam spreading.

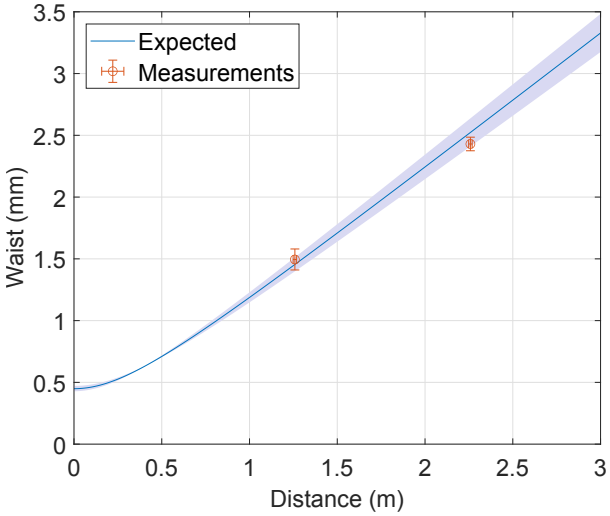

Figure 13: Measured beam waist vs. prediction based on fiber and collimator manufacturing specification

4 Payload Mechanical Design Developments

The mechanical design has slightly grown to better manage the complex optical fiber path that is used in the CLICK-A payload. There are 14 separate fiber optic components and there is 13 splices that are needed to fully connect all the optical fiber components that modulate and monitor the optical power generated during operation. As this optical fiber train was being reviewed by the team, it was realized that there was no way to assure that the minimum bend radius of all the fibers was respected. If the radius of the fiber bending was allowed to go below their listed minimum bend radius, a potentially significant amount of the light can be lost. To assure all the fibers did not bend more than allowed, a fiber raceway was built to route all the fibers in the payload. To connect the fibers, the Diamond Micro Interface connectors were chosen for the ability to swap components easily and the low insertion loss between connections, compared to the fiber splicing machine we had within our lab. A prototype was 3D printed and test fiber was routed to see what design changes needed to be done. A picture of the first prototype is shown in Figure 14.

Figure 14: First Iteration of Fiber Raceway Prototype

After test routing fiber in the raceway, the channels that allowed fiber to wind around the raceway were widened and another prototype was made out of metal. This version had the actual fiber components mounted into it and the components optical fibers were attempted to be routed. The prototype of the first metal raceway is shown in Figure 15.

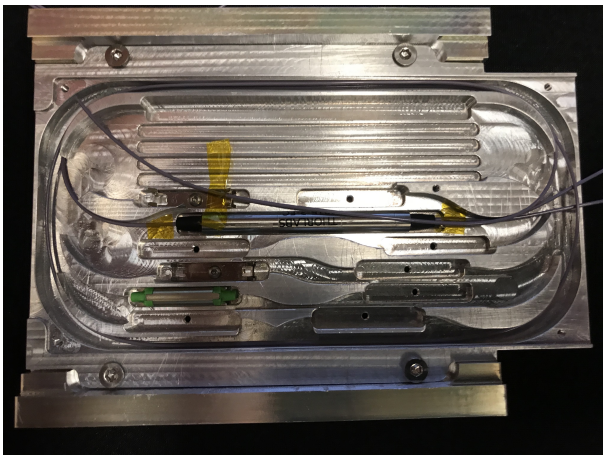

Figure 15: Second Iteration of Fiber Raceway Prototype

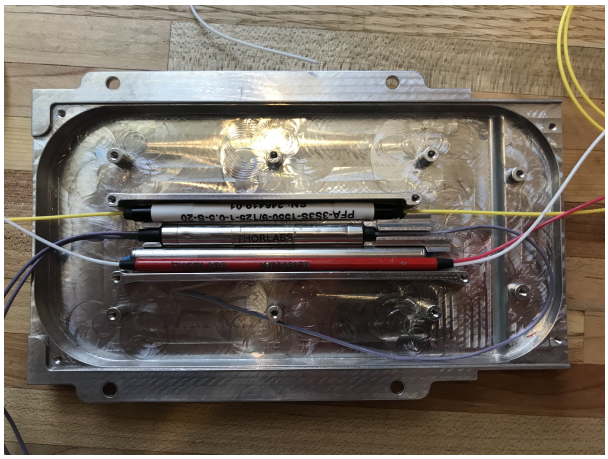

Figure 16: Third Iteration of Fiber Raceway Prototype

While routing, it was determined that defined optical fiber paths made it much more difficult to try to route each fiber. With exact fiber paths, providing the optical fiber connector manufacturer (Diamond) exact lengths of fiber between components that they would need to attach their connectors to proved to be beyond the scope of what we could do for the number of connections that needed to be made. With the difficulty of determining exact fiber lengths and the amount of fiber connections that needed to be made, it was determined that a new method for connecting fibers needed to be found. After searching, a facility on campus happened to be have a fiber splicing machine (Vytran GPX3000) that was suitable for splicing fibers with the loss we required. With the adoption of the new way to connect fibers and the difficulty encountered with routing exact fiber paths, a new fiber raceway was designed. The new raceway has been prototyped, as shown in Figure 16, and the optical fiber components have been determined to fit in their respective positions in the raceway. To maintain the bend radius of each fiber, Kapton tape will be used to tape the fiber down to the raceway with a specific bend radius.

The team is now waiting to get back on campus to finish the training for the optical fiber splicing machine and do a full test of the spliced optical fiber path fitting in the raceway and the performance at modulating the 1550 nm light.

The payload also has had a optical fiducial added to provide a reflective surface for the bus provider to determine the alignment between the payload aperture and the star tracker. This alignment is important since it is needed to assure that the laser being transmitted is pointed correctly by the bus, so the payload can acquire the tracking beacon and be able to transmit towards the ground station.

5 Payload Thermal Design

The thermal model for CLICK A has been rebuilt to standardize the methodology of how the models were built for both the CLICK-A payload as well as the CLICK-B/C payloads. This was pursued since the two payloads, being so similar in mechanical design and mounting to their respective spacecraft, previously had different thermal model assumptions and techniques for simulating the heat loads that define the operation of the payload.

The thermal design is mostly passive except for the heaters to get components up to operational temperatures during the cold case. An important aspect in the thermal design of the CLICK A payload is the specification of which components to use in the custom electronics built for the payload. Originally, the CLICK A payload was not planning on using industrial grade electronic components, but it was determined that certain components had too limited of operational temperature range compared to the temperature range that the bus provider could reasonably maintain. Industrial grade electronic com-

ponents traditionally have an operating range from -40° C to 85° C.

Industrial grade electronic components were chosen, to assure the heater critical components would be able to turn on the payload heaters when necessary. Industrial grade electronic components traditionally have an operating range from -40° C to 85° C. A table of the survival and operational maximum and minimum temperatures is shown in Table 6. One particular component that was of concern was the mvBlueFOX-MLC205G-XOW-2111 camera since the manufacturers data sheet states the lower operational temperature limit to be 0° C. As discussed above, the camera was tested to a temperature -40° C to 40° C and operated as expected.

Table 6: Temperature Limits of Each Component

Component:	Temperature Limits of Each Component (°C)			
	Survival		Operational	
	Min	Max	Min	Max
Daughter Board	-55	125	-25	85
FPGA Board	-40	125	-40	85
Photodiode Board	-40	85	-40	85
CPU Board	-55	125	-40	85
TOSA Board	-40	85	-5	75
Feedback Laser	-35	80	0	60
EDFA	-20	65	0	65
Camera	-40	60	-40	45
FSM	-40	125	-40	125

The thermal model was built from the mechanical CAD model of the CLICK A payload. It is modeled in Thermal Desktop by Cullimore and Ring Technologies. A picture of the thermal model next to the CAD model can be seen in Figure 17. The components of the payload can not be fully represented by the solid shapes that Thermal Desktop models are made of. Whenever possible, the geometry of components was modeled in the thermal model as it is in reality, but if the exact geometry could not be modeled, the correct thermal capacitance was modeled for all components.

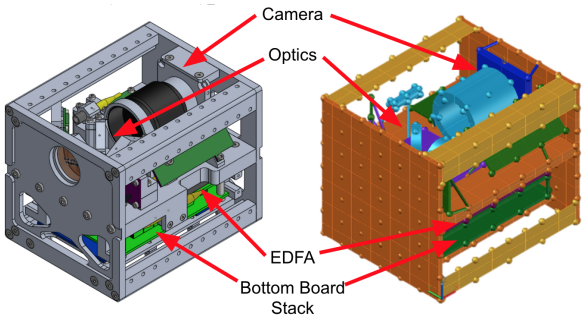

Figure 17: CAD Model Compared to Thermal Desktop Model

As important as modeling the components that make up the payload with the correct thermal capacitance, it is also important to model the boundary conditions and heat loads of the model correctly. The boundary conditions of the model are time varying temperature defined nodes with the profile of the hot and cold boundary conditions provided by the bus provider. The interface between the payload and the spacecraft was defined between -10° C and 25° C. To model the heat loads, the team had to determine exactly what the concept of operations (CONOPs) would look like for a transmission. An outline of the modes that the payload goes through during a transmission as well as the heat dissipated by each component during that mode is shown in Table 7.

Table 7: Heat Loads for Each Mode of Payload Downlink Transmission

Component:	Power Draws (W) for Each Mode		
	Start Up (10 Minutes)	Transmit (15 Minutes)	Power Down (5 Minutes)
Daughter Board	0.4	2	0.4
FPGA Board	1.1	2	1.1
Photodiode Board	0.35	1	0.35
CPU Board	1.5	2	1.5
TOSA Board	0.15	1	0.15
Feedback Laser	0	1	0
EDFA	0	6	0
Camera	0.45	1	0.45
Heaters	5	0	0
Total	**8.95**	**16**	**3.95**

These time dependent heat loads were input into the thermal model to assure that the temperatures that the components become during operation is within their operational temperature bounds. A 10° C margin was kept between all survival component temperature rating, to assure that the payload survives all thermal environments possible on orbit. The predicted temperatures of the components all maintain the margin outlined. The next step is to

run thermal balance and thermal cycling tests for the assembled payload.

6 Payload Electronics Testing

During the summer of 2019 our team went through the electronics to evaluate the current design and functionally tested each board in isolation as best as possible to identify which functionally worked and to develop a more granular set of requirements for the payload as we took on new requirements from our bus provider BCT. At this point we realized that there was a shortcoming in the design specifications laid out previously for Photodiode board and decided that we needed to make changes to improve the functionality of a couple of the other peripheral drive circuits. Just before the end of 2019 our team conducted some bench level system tests to evaluate the updated architecture and functionality of the transmitter electronics. In this section we will go through those changes and provide an updated view on the current functionality of the electronics design.

6.1 Transmit test

In December of 2019 our team set up our new hardware to conduct a transmit test. Coming out of those tests our team came up with a short list of changes that resulted in us adding additional features, redesigned the layout of certain boards and changing the design of a couple of different drive circuits. The most prominent change required was in the layout of the Photodiode board, which after a redesign, continued to prove to be a sticking point. We decided on a design that can be seen schematically in Figure 18 utilizing the LT6268-10 due to its high bandwidth and gain capabilities. However, we needed the maximum performance of this chip and unfortunately, did not pay close enough attention to the layout which hindered performance on the board. Additionally, the part itself claims to have rail-to-rail output capability, but in fact is not able to output anything lower than 80mV. This was not discovered until after we had the boards back from fabrication and resulted in in proper operation for our application.

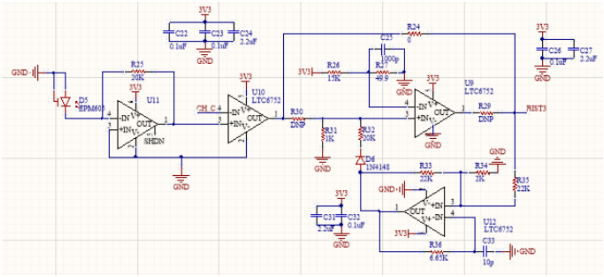

Figure 18: Transimpedance Amplifier design

Fortunately, we were able to get a development board for the LTC6268-10, the DC2414A, that allowed us to quickly address both issues and validate that those changes would result in proper operation. By using the development board we were able to address parasitic capacitance issue that we experienced in the previous design's layout. The development board also provided 3 different layouts optimized for different operating regimes, low, middle and high transimpedance gain, which was great as we could check our design under different optical powers. Using the development board allowed us to connect a virtual ground to the negative input terminal to raise the negative input above the Vol of 80mV and return the part to its normal operating regime. After validating the performance of the development board, after making this change, we closely examined the footprint of the board and used this to inform our follow up redesign of this board.

Unfortunately, without a working Photodiode board, we were not able to functionally validate our transmitter as it critically depends on the feedback that the photodiodes provide. Figure 19 shows the topology of our transmitter design and the integral role that the photodiode's play. Our transmitter utilizes a Fiber Bragg Grating to convert the wavelength modulation of the seed laser into an amplitude modulation scheme and without a working Photodiode board, it is not possible to properly match the wavelength of the seed laser to the FBG in order to translate between the modulation schemes. However, once we have this board updated, we should be able to functionally validate our transmitter and complete final testing.

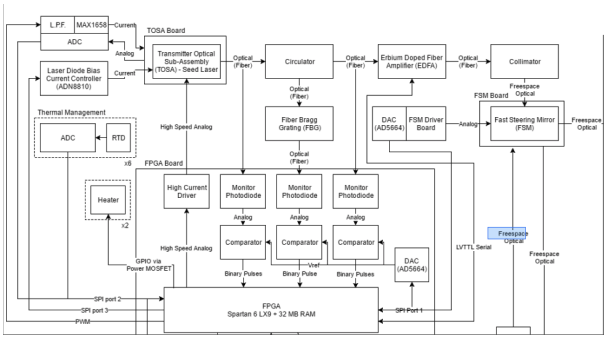

Figure 19: Transmitter Design

6.2 Bus integration changes

As our team continued to test and validate other parts of the payload and discussions with BCT moved forward, several different requirements were refined. Some of these refinements impacted the electronics design, most notably the payload interface and thermal requirements for the payload. Following negotiation with BCT as to the interface functionality we needed and what they were able to provide, we agreed to the interface pin-out that can be seen in Figure 20. We were certainly happy with the final product, but it did require changes to the payload interface as the current design utilized single ended signals on both the SPI and UART bus lines. After completing an interface redesign due to an on orbit CPU reflashing requirement, this was a schedule setback, but certainly a necessary change.

#	Name	Type		#	Name	Type
1	SPI CLK-	LVDS Bus output		17	UART IN+	LVDS Bus input
2	SPI CLK+	LVDS Bus output		18	UART IN-	LVDS Bus input
3	SPI MISO-	LVDS Bus input		19	UART OUT+	LVDS Bus output
4	SPI MISO+	LVDS Bus input		20	UART OUT-	LVDS Bus output
5	SPI MOSI-	LVDS Bus output		21	1PPS PL[3]	Not connected or Bus I/O
6	SPI MOSI+	LVDS Bus output		22	1PPS BUS	LVCMOS 3V3 Bus output
7	SPI CS-	LVDS Bus output		23	EDFA[4]	LVCMOS 3V3 Bus I/O
8	SPI CS+	LVDS Bus output		24	BEACON[5]	LVCMOS 3V3 Bus I/O
9	SWUPDATE[1]	LVCMOS 3V3 Bus I/O		25	RESET[1]	Open collector, Bus output
10	SPARE1[6]	LVCMOS 3V3 Bus I/O		26	SPARE2[6]	LVCMOS 3V3 Bus I/O
11	Ground	Power		27		
12				28		
13				29	Ground	Power
14	Vbat	Power, 9V to 17V		30		
15				31		
16				case	Not connected	

Figure 20: Payload to Bus Interface Pinout

After our team completed additional work on the thermal model for the payload, which can be seen in section 5, it became clear that the operational bounds of the payload needed to be expanded. As can be seen in Table 6 the payload has wide operating temperatures; however, we were previously limited by a small set of a components on the lower temperature bound, which placed it at 0C. This higher lower limit drove an exceptional amount of power consumption and limited the payload's operational window. While there were other components, most notably the camera, that were specified to operationally work above 0C, they were able to be tested in TVAC below their rated temperatures and operated nominally. Fortunately for other components, most of them had drop in industrial grade replacements with expanded operational ranges down to -40C. There was just one component, the XR22404 USB Hub that did not have a drop in replacement. We ended up replacing this part with Microchip's USB2422 which has a operational thermal range of -40C to +85C.

6.3 New features required from testing

Among changes made in the previous sections, some of the operational tests our team completed led to a few additional features being requested that drove changes in the electronics. When our team completed the TVAC testing for the camera, the camera had to be rebooted periodically as it would lose functionality, for seemingly no clear underlying reason. However, the current electronics did not have the ability to reset the camera without the entire payload switching off and so we moved to include a switch that would allow us to reset the camera in case of a failure or lockup. Additionally, when testing the calibration laser, its operational set point drifted beyond the bounds specified and its output power accordingly drifted outside of its specified operational range. As this is an important part of our PAT system, we moved to include both current regulation electronics as well as output power regulation to better control the calibration laser. With these last functional updates to the electronics we froze our development to maintain appropriate schedule and incorporate all of the necessary changes to guarantee appropriate on orbit functionality.

7 Continued Development of the Optical Ground Station

The CLICK A downlink will be received by an optical ground station located at MIT Wallace Astrophysical Observatory in Westford, Massachusetts. The optical ground station is called the Portable Telescope for Lasercom (PorTeL), and it consists of a 28 cm diameter aperture Commercial-Off-The-Shelf (COTS) amateur telescope that has been modified to carry a lasercom receiver and a beacon uplink laser. A systems architecture diagram is shown in Figure 21.

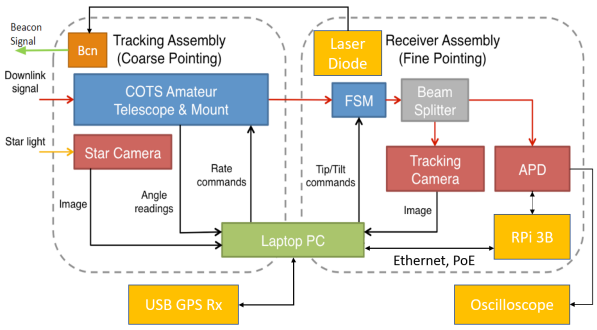

Figure 21: PorTeL Architecture.[2,3]

This architecture enables the concept of operations as follows. First, prior to operations, the telescope coordinate system is calibrated relative to the Earth reference system using the star camera and GPS receiver. This enables open-loop tracking of the CLICK A spacecraft using telemetry data from its onboard Global Positioning System (GPS) receiver and/or Two-Line Elements (TLEs) provided freely online by the USAF's Joint Space Operations Center (JSpOC). As discussed previously, the beacon laser source power and divergence are designed such that the expected open-loop pointing error is sufficiently small to enable detection of the beacon source by the CLICK A payload camera, which is body-pointed towards the PorTeL's geodetic coordinates with an accuracy well within its 10° field of view. Once the beacon is detected by the payload, the payload's fine pointing system activates, which provides sufficient pointing accuracy of the downlink laser to enable detection by PorTeL's InGaS Tracking Camera. The Tracking Camera is used to engage closed-loop tracking of the satellite, which occurs in two stages. First, the centroid offset data from the camera is directly used to provide feedback to the gimbals. Second, the Fine Steering Mirror (FSM) engages to maintain precise alignment of the received signal onto the 200 μm diameter active area of the Avalanche Photodiode Detector (APD), which is used to receive the lasercom data. For the CLICK A mission phase, the APD signal is routed to an oscilloscope to collect snapshots of raw data that are then post-processed to validate the mission requirement of a $\geq$10 Mbps downlink. For the CLICK B/C mission phase, the demodulator that is currently being developed for the CLICK B/C payload will be adapted for ground use to enable real time demodulation of the downlink signal. For more detail on the conception of PorTeL in addition to the design, development, and testing of the Pointing, Acquisition, and Tracking (PAT) system that was briefly described here, the reader is referred to *Riesing* and *Riesing et al.*[2,3]

In the following, a summary of the recent development efforts of the receiver assembly and the beacon uplink laser will be given.

7.1 Ground Lasercom Receiver Optomechanical Development

One of the major development areas of the PorTeL optical ground station has been the optomechanical design. The current design is shown in Figures 23. The current prototype unit is shown, which has been manufactured and assembled according to the CAD design shown to its right. The design identifies the major components, which include the electro-optical components discussed previously. The design also includes several COTS optics to direct the received signals onto these electro-optical components. Figure 25 shows the optical paths via section views. The light that is received by the telescope is directed into a baffled bore in the base where the receiver assembly is mounted. A Keplerian beam expander with a 2.62x angular magnification (in the receive direction) is mounted inside this bore. The FSM is mounted at the exit pupil of the beam expander, which prevents the receive signal from "walking off" the FSM, which was noted as an issue in the prototype designed by Riesing.[2] The exit of the beam expander also contains a 1550 nm CWL, 12 nm FWHM bandpass filter to reduce the background optical noise entering the system to improve SNR on the receivers. This filter will be swapped with a dual-bandpass filter for the CLICK B/C downlink, which has an additional requirement to receive a 976 nm beacon downlink signal. The beam expander is concentrically mounted to a bore in the main fixturing plate to ensure alignment with the FSM within machine tolerances, which is sufficient for assembly. The beam is 50:50 split (TBR - link budget) between the camera and the APD. Lastly, a 40 mm focal length lens is used to focus the received signal onto each of the sensors.

The FSM itself is mounted on a tip/tilt kinematic mount. Further kinematic mounts in the design include a X/Y translation mount for the APD and an additional tip/tilt mount for the beacon collimator, which is mounted on the bore of the telescope. These kinematic mounts allow for systematic and precise alignment of the optical elements according to the following calibration steps. First, the beacon is directed towards a retroreflector mounted in front of the payload that is sufficiently large to provide a vertical displacement of the beacon signal prior to reflection that allows the telescope to receive the signal. The FSM is then aligned such that the cen-

troid of this signal is centered in the Tracking Camera. This first step aligns the beacon path with the camera's receive path, which minimizes bias errors due to misalignment in the beacon pointing during closed-loop tracking. Second, the beacon is turned off, and a 1550 nm source collimated by an Off-Axis Parabolic (OAP) mirror is aligned with the telescope such that the receive signal is centered in the camera. The APD is then adjusted in decentration using the X/Y kinematic mount. An oscilloscope connected to the APD's board is used to take traces of the receive signal, which has been empirically calibrated against known received power values as part of the CHOMPTT mission.[19] This enables adjustment of the APD to minimize implementation losses by maximizing received measured power. Sufficient alignment of the APD is achieved when measured implementation losses are less than TBD dB (see link budget).

7.2 Ground Beacon Laser Development

An important element of PorTeL that was not developed in previous work is the beacon uplink laser.[2,3] The selected specifications balance the requirements against the availability of COTS components. The selected laser diode is a Gooch & Housego EM336, which is a multimode fiber-coupled diode with a CWL of 975 nm and an output power of 5 W. The laser diode is mounted to a custom board on the receiver assembly that is flush against a heat sink connected to the main aluminum structure. The brackets holding the receiver assembly to the telescope were chosen to be aluminum to allow heat to flow to the much larger heat sink of the telescope backend to mitigate thermoelastic shifts of the optical fixturing. It should be noted that the laser diode location was chosen to be on the receiver assembly because it is comoving with the telescope, which avoids potential bend losses due to fiber wrapping issues while slewing.

The diode is fiber-coupled to an adjustable collimator, which will be mounted on the bore of the telescope. Since the diode has multimode output and is coupled into a multimode fiber, degraded beam quality (M^2) has to be taken into account when predicting the beam divergence out of the collimator. If the diode output clips the fiber at the coupling interface, it can be assumed that the power will be equipartitioned across all the guided modes of the fiber at the collimator interface. The beam M^2 can then be approximated as follows:

$$M^2 \approx \frac{\pi r_{core} \mathrm{NA}}{\lambda} \tag{2}$$

where r_{core} is the fiber core radius, NA is the fiber numerical aperture, and λ the wavelength. Using the parameters of the EM336 diode yields an $M^2 \approx 25$. Since this M^2 value is fairly uncertain and it is also important to have flexibility in terms of the uplink beacon divergence, it was decided to use an adjustable collimator with large enough adjustment range to accommodate the fairly large divergences on the order of tenths of a degree needed. Figure 26 shows the predicted full-width half-maximum (FWHM) divergence from an adjustable ZC618APC-B zoom collimator from Thorlabs. It can be seen that the collimator supports a FWHM range of about 0.2°-0.6° for $M^2 = 25$, which is a broad enough range to meet our requirements. This analysis will be verified by testing the collimator in the optics lab prior to deployment on the portable telescope.

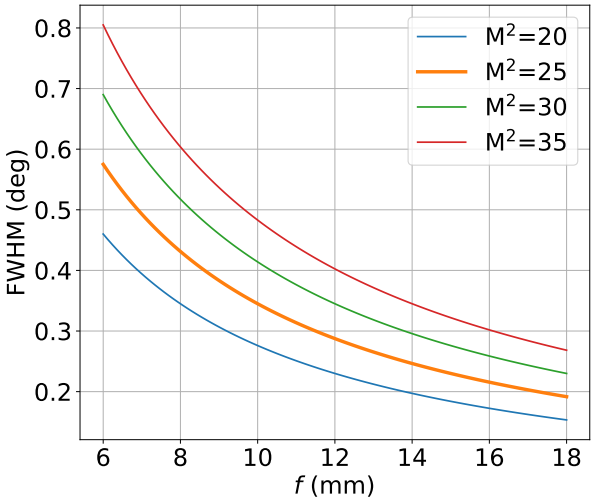

Figure 26: Predicted FWHM divergence from the ZC618APC-B collimator

An additional benefit of using an adjustable collimator is that it enables optimization of uplink performance by setting the beam divergence according to available information in the uplink pointing budget discussed previously. The variability of the total pointing error is mainly due to the variability in the error component contributed by orbit determination errors, which, as discussed previously, can vary significantly depending on the availability and quality of GPS telemetry data and/or TLE data during operations. The optimal divergence can be derived from the information in the pointing budget as follows.

There are two terms in the link budget equation that are functions of the divergence angle: the pointing loss ($L_{\mathrm{ptg,dB}}$) and the transmit gain ($G_{\mathrm{Tx,dB}}$).

Therefore, the objective function to be maximized ($J(\theta_{1/e^2})$) can be defined as a simplification of the expression for received power ($P_{\text{Rx,dB}}$) as follows.

$$J(\theta_{1/e^2}) = L_{\text{ptg,dB}}(\theta_{1/e^2}) + G_{\text{Tx,dB}}(\theta_{1/e^2}) \tag{3a}$$

$$= -80\text{Log}_{10}(e)\left(\frac{\Theta}{\theta_{1/e^2}}\right)^2 + ... \tag{3b}$$

$$... - 20\text{Log}_{10}(\theta_{1/e^2} + 10\text{Log}_{10}(32) \tag{3c}$$

As $J(\theta_{1/e^2})$ is a random variable, it can be optimized by imposing a reliability probability requirement (p_r) in order to yield a nonrandom objective function. This can be done analytically since the expression for $J(\theta_{1/e^2})$ can be re-arranged into a linear function of a random variable with a known distribution by making this substitution for $\Theta^2 = \sigma^2(\Theta_x^2/\sigma^2 + \Theta_y^2/\sigma^2) \equiv \sigma^2 X$, where $X \sim \chi_2^2(2\mu^2/\sigma^2)$ (i.e. a noncentral chi-squared distribution with two degrees of freedom).[5] For analytical convenience, also define $\bar{J} \equiv -J$.

$$\bar{J} = aX + b \tag{4a}$$

$$a \equiv 80\text{Log}_{10}(e)\left(\frac{\sigma}{\theta_{1/e^2}}\right)^2 \tag{4b}$$

$$b \equiv 20\text{Log}_{10}(\theta_{1/e^2}) - 10\text{Log}_{10}(32) \tag{4c}$$

Therefore, the cumulative distribution function (CDF) of $\bar{J}$ ($F_{\bar{J}}(\bar{j})$) can be related to the CDF of X ($F_X(x)$) as follows.

$$p_r = F_{\bar{J}}(\bar{j}) = \mathbb{P}[aX + b \leq \bar{j}] \tag{5a}$$

$$= \mathbb{P}[X \leq (\bar{j} - b)/a] \tag{5b}$$

$$= F_X((\bar{j} - b)/a) \tag{5c}$$

Hence, the nonrandom objective function $j(\theta_{1/e^2})$ is defined as follows.

$$j = -\bar{j} = -aF_X^{-1}(p_r) - b \tag{6a}$$

$$= -80\text{Log}_{10}(e)\left(\frac{\sigma}{\theta_{1/e^2}}\right)^2 F_X^{-1}(p_r) + ... \tag{6b}$$

$$... - 20\text{Log}_{10}(\theta_{1/e^2}) + 10\text{Log}_{10}(32) \tag{6c}$$

where the inverse CDF of X is evaluated numerically using a statistical math software package. Note that the value of this function depends on μ and σ in addition to p_r, which is denoted by $F_X^{-1}(p_r; \mu, \sigma)$. Setting the gradient of $j(\theta_{1/e^2})$ equal to zero yields the optimal divergence angle (θ^*_{1/e^2}).

$$\theta^*_{1/e^2} = \sqrt{8\sigma^2 F_X^{-1}(p_r; \mu, \sigma)} \tag{7}$$

It should be noted that upon substituting the optimal divergence angle into the pointing loss model, an optimal pointing loss value is found that is independent of the error distribution: $L^*_{\text{ptg,dB}}(\theta^*_{1/e^2}) = -10\log_{10}(e) \approx -4.343$ dB. It should also be noted that if $\mu/\sigma \approx 0$, then Θ can be approximated as Rayleigh distributed $\Theta \sim \text{Rayleigh}(\sigma)$, which leads to an analytical expression for the optimal divergence angle since now $\Theta^2 \sim \text{Exp}(1/(2\sigma^2))$.[5] Performing a similar derivation as in the above leads to an analytical approximation for the optimal divergence angle for the case of small bias errors.

$$\theta^*_{1/e^2} \approx \sqrt{-16\sigma^2 \ln(1 - p_r)}, \ (\mu/\sigma \approx 0) \tag{8}$$

The values for μ and σ are computed using Table 3 with a more conservative requirement value of 1 km (1-σ) ephemeris error. The actual ephemeris error is likely to be larger than the current estimate because the simulation carried out to compute the estimate made several simplifying assumptions that would not be true during actual operations (e.g. approximating an average spacecraft ram area for the drag perturbation rather than plugging in a true attitude configuration sequence). This yields a CSTOL distribution of $N(12.24, 672.9)\mu$rad at the acquisition range, which gives $\theta^*_{1/e^2} = 6488\mu$rad ($\theta^*_{FWHM} = 0.22°$) using Equation 7 with $p_r = 0.997$. With regard to the design $\theta_{1/e^2} = 9487\mu$rad ($\theta^*_{FWHM} = 0.32°$), the factor of safety is about 1.5, and the selected collimator offers a sufficient adjustable range to compensate for changes in the pointing error estimates as the mission continues to mature.

In this section, additional development of the optical ground station, PorTeL, were discussed. These include further development of the optomechanical design of the lasercom receiver unit and the design of a beacon laser system for uplink. Refractive optics were added to the lasercom receiver to improve its performance over previous prototypes: a 2.62x beam expander was added with the FSM at its exit pupil to both reduce the beam diameter to reduced implemetation losses as well as prevent an issue were the receive signal could move off of the FSM and be lost (by definition, the light exiting a beam expander must go through its exit pupil). Additionally, focusing lenses were added to each of the receive sensors to reduce implementation losses and improve their fields of view and compensate for the angular magnification effect of the beam expander ($\pm 0.208°$ x $\pm 0.259°$ FOV for the tracking camera and $\pm 0.013°$ for the APD sensor). The uplink beacon system was designed with a COTS 975 nm CWL, 5 W multimode laser diode fiber coupled to a variable zoom collimator with a divergence range of $0.2° - 0.6°$. The

optimal divergence given the expected open-loop uplink pointing error was computed via statistical analysis to be 9487μrad (0.32° FWHM). The collimator adjustability is essential for agile mission development as more data on uplink pointing performance is collected.

8 Conclusions and Future Work

This paper presented the latest test results and lessons learned from the CLICK-A payload and optical ground station developments.

The results of a survey of overpasses of the CLICK A OGS location from a LEO ISS orbit were used to downselect passes satisfying four metrics: a minimum pass duration of 1 minute, a maximum pass elevation between 20° and 80°, a minimum pass range of less than 1000 km, and a pass time that occurs while the OGS is in eclipse. 23.5% of passes satisfied these metrics with an average waiting time between these types of passes of 15.03 hours. A single reference pass was selected for link analysis with a pass duration was 10.90 minutes, maximum pass elevation of 53.99°, minimum pass range of 517.60 km, and occurring during eclipse of the OGS. Link analysis showed that the beacon uplink budgets closed for a duration of 7.91 minutes. Furthermore, all the communications downlink closed with margin for PPM orders 4 to 128 during the pass with respective durations between 1.17 minutes and 6.5 minutes. The mission requirement of $\geq$10 Mbps is satisfied for PPM orders less than 32. Furthermore, PPM 16 acheived the best theoretical data transfer for a fixed PPM order of 4.507 Gb. Lastly, an improved data transfer of 7.916 Gb could be achieved by optimal variation of the PPM order during the pass. The pointing budget analysis for the OGS beacon laser when operating in open-loop (CSTOL) and closed-loop (CSTCL) coarse stage tracking modes are given as well as the pointing budget for the spacecraft transmit laser operating in fine stage tracking (FST) mode. The 9487μrad $1/e^2$ (0.32° FWHM) uplink beacon divergence coupled with open-loop and closed-loop $3-\sigma$ pointing errors of 1914μrad and 317.3μrad yielded pointing losses of -1.414 dB and -0.039 dB at the time of uplink acquisition. Upon uplink acquisition, the 2208μrad $1/e^2$ (1300μrad FWHM) transmit laser divergence coupled with a closed-loop $3-\sigma$ pointing error of 136.9μ rad yielded a pointing loss of -0.134 dB at the time up uplink acquisition, which is also the time of downlink closure.

The optical system underwent several tests to verify its performance will meet requirements in space. The beacon receiver performance was tested across a wide range of temperatures in vacuum and confirmed that the COTS camera and lens assembly can successfully maintain good enough focus for beacon tracking, with sub-1 dB uplink SNR degradation below a temperature of 30°C. Investigation and surface figure measurement of the double bandpass filter revealed that the one-sided filter coating warps its substrate, causing curvature of several wavelengths, and posing risk of both beacon receiver defocus and transmit beam spreading. The beacon receiver lens assembly has to be re-focused to compensate for this curvature. Measurement of the transmit beam divergence confirmed that impact of the curvature is negligible in terms of transmit beam spreading, showing a very small 0.02 dB change in the system transmit gain. Measurement of the MEMS FSM thermal deformation revealed sub-wavelength defocus beam aberration, which is also negligible in terms of beam spreading for the CLICK-A payload. The updated fiber routing design and thermal models are presented, together with updates on the ground station mechanical design and beacon collimator analysis.

The next steps for CLICK-A include assembly and splicing of the fiber optic chain inside the redesigned fiber raceway, over-the-air testing of the payload flight model transmitter, and vibration and TVAC testing of the fully packaged payload. After this, the payload will be transported to Colorado for integration with the host spacecraft provided by BCT, where it will undergo a final round of testing and preflight checks before the planned early 2021 launch.

Additional development of the optical ground station, PorTeL, was also discussed. These include further development of the optomechanical design of the lasercom receiver unit and the design of a beacon laser system for uplink. Refractive optics were added to the lasercom receiver to improve its performance over previous prototypes: a 2.62x beam expander was added with the FSM at its exit pupil to both reduce the beam diameter to reduced implemetation losses as well as prevent an issue were the receive signal could move off of the FSM and be lost (by definition, the light exiting a beam expander must go through its exit pupil). Additionally, focusing lenses were added to each of the receive sensors to reduce implementation losses and improve their fields of view and compensate for the angular magnification effect of the beam expander ($\pm$0.208° x $\pm$0.259° FOV for the tracking camera and $\pm$0.013° for the APD sensor). The uplink beacon system was designed with a COTS 975 nm CWL, 5 W multi-

mode laser diode fiber coupled to a COTS variable zoom collimator with a FWHM divergence range of $0.2° - 0.6°$. The optimal divergence given the expected open-loop uplink pointing error was computed via statistical analysis to be 9487μrad (0.32° FWHM). The collimator adjustability is essential for agile mission development as more data on uplink pointing performance is collected.

Acknowledgments

The mission is a collaboration between the MIT Space, Telecommunications, Astronomy, and Radiation (STAR) Lab, University of Florida's Precision Space Systems Lab (PSSL), and NASA Ames Research Center (ARC). This work was funded by the CLICK (CubeSat Laser Infrared CrosslinK) Technology Demonstration Mission, Grant Number 80NSSC18K1579. The views, opinions, and/or findings contained in this work are those of the authors and should not be interpreted as representing the official views or policies, either expressed or implied, of the National Aeronautics and Space Administration.

References

[1] Curt Schieler, Bryan Robinson, Owen Guldner, Bryan Bilyeu, Ajay Garg, Kathleen Riesing, Jessica Chang, Farhad Hakimi, Joshua Brown, Farzana Khatri, Steven Constantine, Jamie Burnside, Don Boroson, and Donald Cornwell. NASA's Terabyte Infrared Delivery (TBIRD) Program: Large-Volume Data Transfer from LEO. In *33rd Annual AIAA/USU Conference on Small Satellites*, aug 2019.

[2] Kathleen Riesing. Portable Optical Ground Stations for Satellite Communication. PhD Thesis. Massachusetts Institute of Technology. 2018.

[3] Kathleen Riesing, Hyosang Yoon, and Kerri Cahoy. A portable optical ground station for low-earth orbit satellite communications. *2017 IEEE International Conference on Space Optical Systems and Applications*, 2017.

[4] Website. Iss - orbit. https://heavens-above.com/orbit.aspx?satid=25544. 2020.

[5] Peter Grenfell. GNSS-Based Relative Navigation for LEO Nanosatellite Laser Communications. Master's Thesis. Massachusetts Institute of Technology. 2020.

[6] William L. Casey and Stephen G. Lambert. *Laser Communications in Space*. Artech House Inc, Norwood, 1995.

[7] Emily B Clements. *Probabilistic Methods for Systems Engineering with Application to Nanosatellite Laser Communications*. PhD thesis, Massachusetts Institute of Technology, 2018.

[8] Emily Clements, Derek Barnes, Ryan Kingsbury, and Caleb Ziegler. Nanosatellite optical downlink experiment : design , simulation , and prototyping. 2018.

[9] Ryan Kingsbury. *Optical Communications for Small Satellites*. PhD thesis, Massachusetts Institute of Technology, 2015.

[10] H T Yura. Threshold detection in the presence of atmospheric turbulence. *Applied Optics*, 34(6):1097–1102, 1995.

[11] Ondrej Cierny. Precision Closed-Loop Laser Pointing System for the Nanosatellite Optical Downlink Experiment. 2017.

[12] David A. Vallado and Paul Crawford. SGP4 orbit determination. *AIAA/AAS Astrodynamics Specialist Conference and Exhibit*, (August), 2008.

[13] Oliver Montenbruck. An epoch state filter for use with analytical orbit models of low earth satellites. *Aerospace Science and Technology*, 4(4):277–287, 2000.

[14] Erin Kahr, Oliver Montenbruck, and Kyle P. G. O'Keefe. Estimation and Analysis of Two-Line Elements for Small Satellites. *Journal of Spacecraft and Rockets*, 50(2):433–439, 2013.

[15] Joel Shields, Christopher Pong, Kevin Lo, Laura Jones, Swati Mohan, Chava Marom, Ian Mckinley, William Wilson, and Luis Andrade. Characterization of CubeSat Reaction Wheel Assemblies. *Journal of Small Satellites*, 6(1):565–580, 2017.

[16] James Paul Mason, Matt Baumgart, Bryan Rogler, Chloe Downs, Margaret Williams, Thomas N. Woods, Scott Palo, Phillip C. Chamberlin, Stanley Solomon, Andrew Jones, Xinlin Li, Rick Kohnert, and Amir Caspi. MinXSS-1 CubeSat On-Orbit Pointing and Power Performance: The First Flight of the Blue Canyon Technologies XACT 3-axis Attitude Determination and Control System. 2017.

[17] Ondrej Čierny and Kerri L. Cahoy. On-orbit beam pointing calibration for nanosatellite laser communications. *Optical Engineering*, 58(04):1, nov 2018.

[18] Paula do Vale Pereira, Matthew T. Hunwardsen, and Kerri Cahoy. Characterization of laser thermal loading on microelectromechanical systems-based fast steering mirror in vacuum. *Optical Engineering*, 59(05):1, may 2020.

[19] John Conklin, Seth Nydam, Tyler Ritz, Nathan Barnwell, Paul Serra, John Hanson, Anh Nguyen, Cedric Priscal, Jan Stupl, Belgacem Jaroux, and Adam Zufall. Preliminary Results from the CHOMPTT Laser Time-Transfer Mission. In *Proceedings of the AIAA/USU Conference on Small Satellites, SSC19-VI-03.*, 2019.

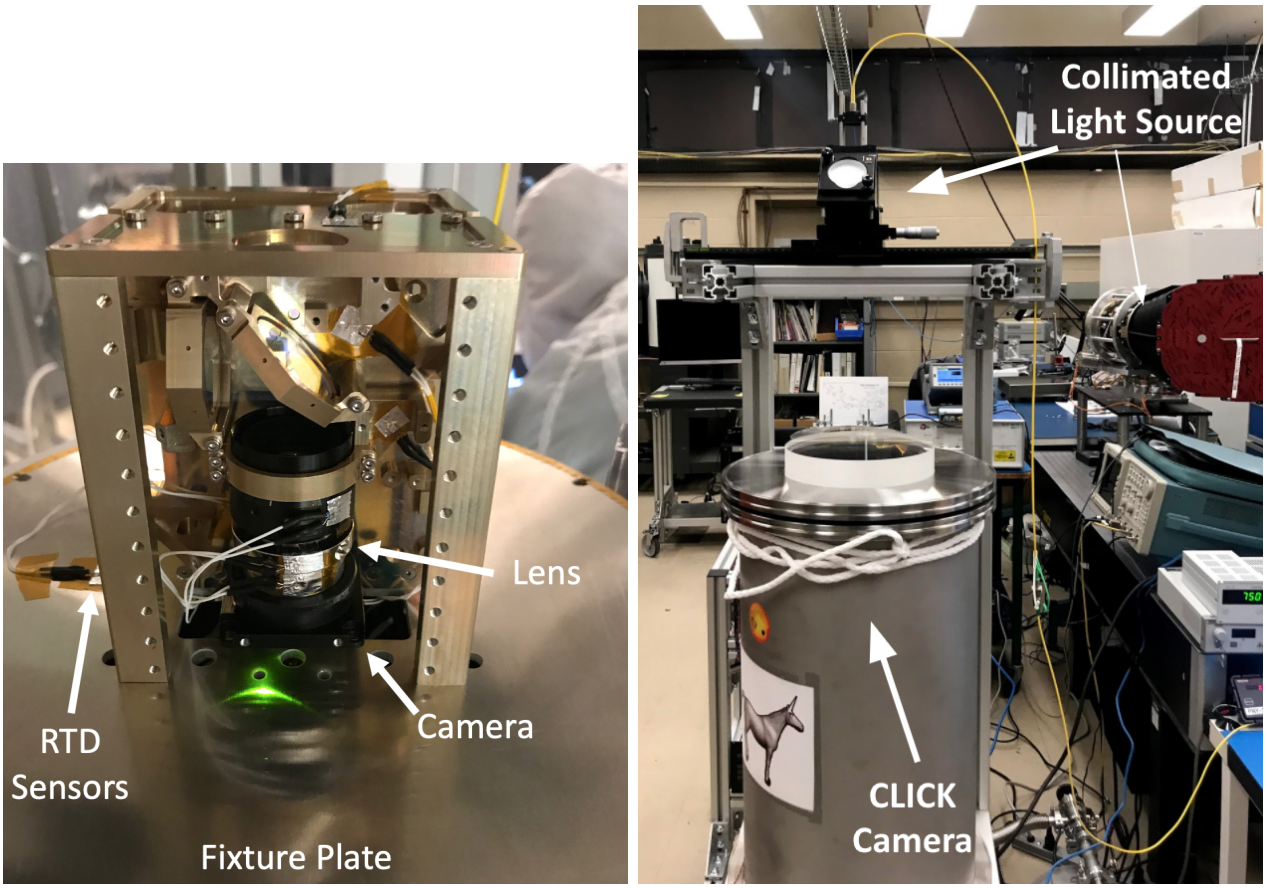

Figure 9: a) Camera and Lens Mounting Fixture. b) Camera and Lens TVAC Setup.

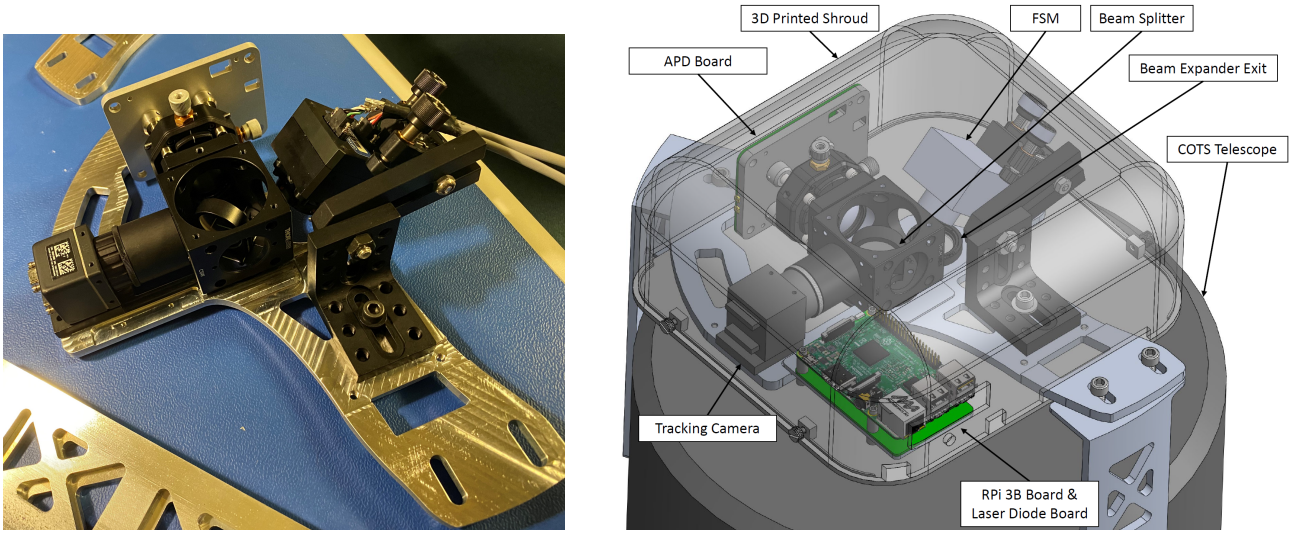

Figure 23: a) Ground Lasercom Receiver Prototype in Development. b) Ground Lasercom Receiver Isometric View.

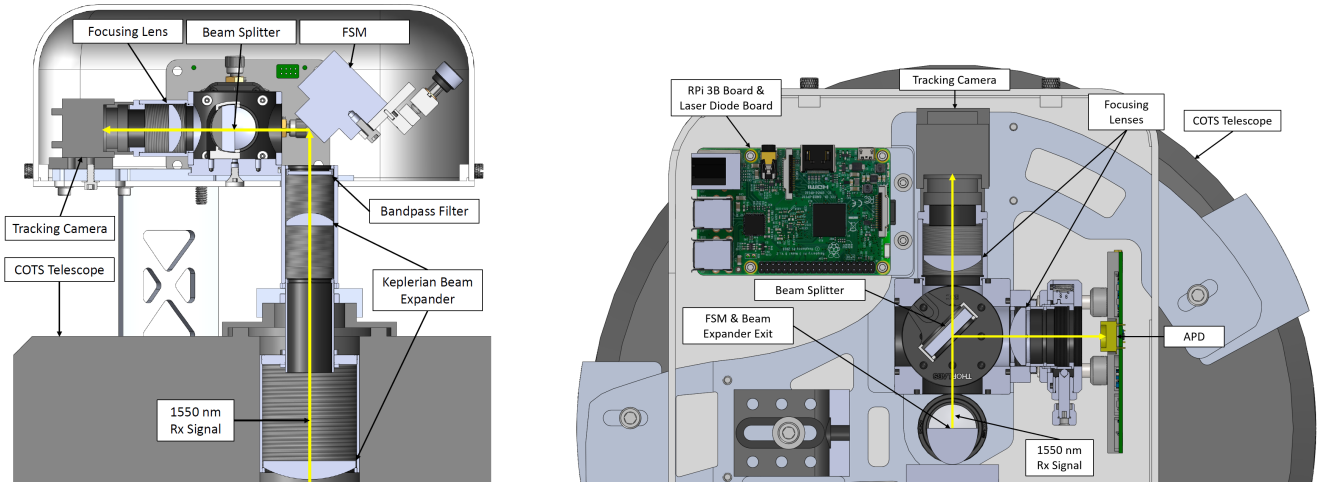

Figure 25: a) Ground Lasercom Receiver Optics Side Section View. b) Ground Lasercom Receiver Optics Top Section View.